PhotoniX

RESEARCH Open Access

Event-based optical imaging and reconstruction of in vivo neuronal and vascular dynamics

Jongmin Yoon[1,2†], Soi Kim[3†], Seungjae Han[3†], Minho Eom[3], Eun-Seo Cho[3], Fatemeh Dehghan Nezhad[5], Soojung Hong[1,2], Eunjee Kim[1,2], In-Hyun Park[6], Euiheon Chung[5,7*], Kunyoo Shin[1,2*], Young-Gyu Yoon[3,4*] and Myunghwan Choi[1,2*]

†Jongmin Yoon, Soi Kim and Seungjae Han contributed equally to this work.

*Correspondence: ogong50@gist.ac.kr; kunyoos@snu.ac.kr;ygyoon@kaist.ac.kr; choim@snu.ac.kr

[1] School of Biological Sciences, Seoul National University, Seoul 08826, Republic of Korea
[2] The Institute of Molecular Biology and Genetics, Seoul 08826, Republic of Korea
[3] School of Electrical Engineering, KAIST, Daejeon, Republic of Korea
[4] KAIST Institute for Health Science and Technology, Daejeon, Republic of Korea
[5] Department of Biomedical Science and Engineering, Gwangju Institute of Science and Technology, Gwangju, Republic of Korea
[6] Department of Genetics, Yale Stem Cell Center, Yale School of Medicine, New Haven, CT 06520, USA
[7] AI Graduate School, Gwangju Institute of Science and Technology, Gwangju, Republic of Korea

Abstract

Event cameras, which asynchronously detect local brightness changes with sub-millisecond precision, offer high temporal resolution, wide dynamic range, and efficient data throughput. While these advantages have driven advances in dynamic vision and motion analysis, their application to functional biological imaging remains underexplored. Here we present a comprehensive event-based imaging framework that includes quantitative optical characterization of event cameras, multi-modal in vivo imaging including cortical blood flow and neuronal calcium dynamics, and a novel self-supervised reconstruction algorithm, Implicit Neural Factorization (INF), which converts sparse event streams into continuous activity signals. This framework opens new possibilities for high-resolution, data-efficient functional imaging in biology.

Keywords: Event-based imaging, Neuronal calcium dynamics, Implicit neural factorization, Functional biological imaging, Self-supervised learning, Asynchronous sensing

Introduction

Understanding brain function demands tools capable of monitoring neuronal activity with exceptional spatiotemporal precision. Optical imaging has become an indispensable technique in neuroscience for this purpose, enabling non-contact, high-resolution visualization of large-scale neuronal populations at subcellular levels [1, 2]. However, conventional high-speed imaging faces intrinsic trade-offs between spatial and temporal resolution. Increasing frame rates reduces the field of view or spatial resolution—through subarray readout or pixel binning—thereby introducing crosstalk between features [3]. Additionally, shorter exposure times diminish the signal-to-noise ratio due to reduced photon counts, while stronger illumination accelerates photobleaching, hindering stable, long-term imaging [4, 5]. Moreover, because neuronal activity is inherently sparse [6, 7], traditional frame-based acquisition produces massive data volumes with

Springer

low information density, often exceeding 1 GB/s, thereby posing challenges for real-time data storage, transfer, and analysis [8].

Event cameras offer a promising alternative for overcoming these limitations. Unlike conventional frame-based sensors that synchronously sample all pixels at fixed frame rates, event cameras asynchronously detect local brightness changes with sub-millisecond precision, generating an event when the logarithmic intensity changes at a pixel exceeds a preset threshold. This architecture enables ultra-high temporal resolution, a high dynamic range exceeding 110 dB (compared to 50–60 dB for sCMOS), and substantially lower data rates and power consumption. Leveraging these unique features, event cameras have recently been applied in various biological applications, including single-molecule localization microscopy [9], light-field microscopy for kilohertz-rate volumetric reconstructions [10], neuromorphic cell sorting [11], event-guided synchrotron X-ray imaging [12], and hybrid event/CMOS fluorescence microscopy [13].

Although the sparse and dynamic nature of neuronal activity aligns naturally with the asynchronous sampling paradigm of event cameras, a comprehensive framework for functional biological imaging using these sensors has not been established. Notably, most existing event-based techniques have focused on motion or blinking signals, where large brightness changes ($\Delta F/F_0 \gg 1$) enable robust event detection [9–13]. In such settings, the reconstructed data primarily captures where brightness changes occurred, rather than precisely recovering the magnitude and temporal dynamics of intensity changes. In contrast, functional imaging of neurons poses a substantially more challenging scenario. Brightness changes arising from functional indicators are inherently smaller ($\Delta F/F_0 \approx 0.1$–0.5) than those encountered in motion or blinking applications, and illumination intensity is further constrained by photobleaching and phototoxicity, limiting attainable signal amplitude and signal-to-noise ratio.

Accordingly, a comprehensive pipeline should begin with quantitative optical characterization of event cameras under biologically relevant criteria, to assess whether a given imaging modality is compatible with event-based acquisition. Subsequently, compatible imaging modalities should be experimentally validated, followed by the development of reconstruction algorithms capable of converting discrete event streams into analyzable representations [1, 14–17]. Such a pipeline would delineate the practical scope of event-camera-based functional imaging and enable the translation of sparse event data into quantitative biological readouts with a large field-of-view with maximum 5 kHz acquisition.

In this work, we present a unified framework for functional imaging with event cameras —encompassing optical characterization, modality validation, and data reconstruction. We first quantified the optical performance of event cameras and determined the $\Delta F/F_0$ threshold required to achieve a target signal-to-background ratio (SBR) under biologically plausible irradiance levels. Guided by this analysis, we then performed event-based imaging of cortical blood flow and neuronal calcium dynamics across multiple biological systems, including cultured neurons, brain organoids, and the intact mouse cortex in vivo. Finally, we developed a self-supervised reconstruction method, Implicit Neural Factorization (INF), to convert discrete, asynchronous event streams into continuous, high-resolution activity traces. This biologically informed approach performs substantially better than existing self-supervised reconstruction methods when applied

to real calcium imaging data, without attenuating $\Delta F/F_0$ or introducing strong noise, faithfully recovering the amplitude and timing of individual calcium transients.

Results

Optical characterization of the event camera

To test the feasibility of using event cameras for functional biological imaging, we first performed a systematic optical characterization. We constructed an inverted widefield microscope equipped with a programmable LED module in the excitation path (Fig. 1a). In the detection path, we installed an event-based camera and an sCMOS camera. The light path was controlled by either a beamsplitter (event camera: sCMOS = 8:2) or a flip mirror, with a 0.55 × demagnifier to increase the field of view of the event camera by a factor of ~ 3.3. We used the DVXplorer (iniVation), whose high dynamic range and stable contrast threshold behavior made it a suitable representative model for quantitative optical characterization.

Unlike conventional sCMOS cameras that continuously measure absolute brightness, event cameras emit either a positive (+1) or negative (−1) event whenever the logarithmic change in brightness at a pixel exceeds a preset threshold. This results in the event camera encoding the temporal derivative of the input signal rather than its absolute intensity. Under triangular-wave illumination, the sCMOS trace follows the input intensity, f(t), whereas the event camera output corresponds to its temporal derivative, df(t)/dt, showing high positive polarity during brightness increases and vice versa (Fig. 1b, c).

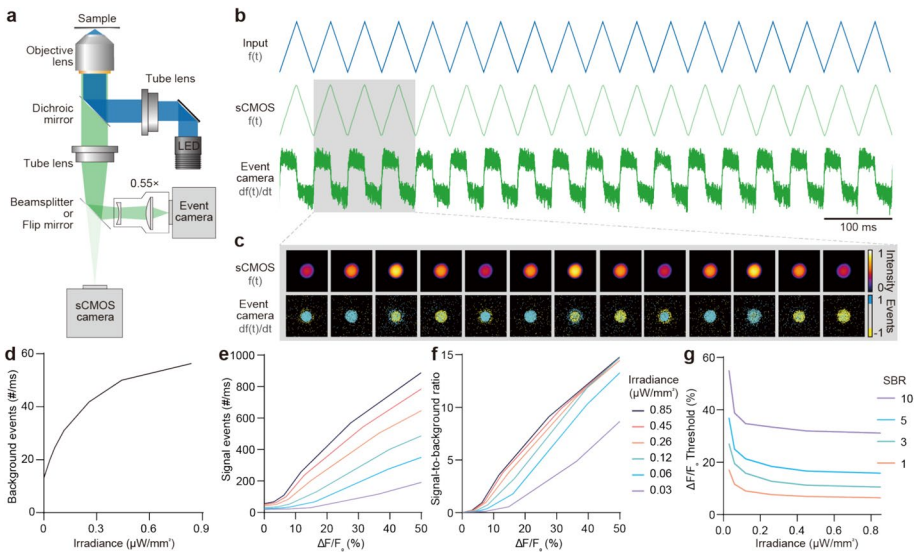

Fig. 1 Optical characterization of event camera performance for functional imaging. **a** Schematic illustration of the optical configuration. **b** Comparison of sCMOS and event camera responses under 20 Hz triangular-wave input illumination. The sCMOS sensor records continuous brightness over time, whereas the event camera detects discrete increases and decreases in brightness. Only positive events are displayed for clarity. **c** Representative images of sCMOS and event camera output. **d** Background event rate measured under stable illumination at increasing irradiance levels. **e** Event rate plotted against relative brightness change ($\Delta F/F_0$) for different irradiance levels. **f** Signal-to-background ratio (SBR) as a function of $\Delta F/F_0$ and irradiance, revealing improved contrast with larger signal changes and brighter illumination. **g** Minimum $\Delta F/F_0$ to achieve a target SBR plotted across different irradiance levels. Higher irradiance reduces the detection threshold, indicating improved sensitivity

To determine optimal conditions for biological imaging, we quantified event generation and background activity under varying irradiance and relative brightness change ($\Delta F/F_0$). Imaging was performed using the 'High' sensitivity (threshold = 5) configuration, which provided the best balance between background suppression and sensitivity (see Fig. S1 for detailed comparison). Background event rates under stable illumination increased with higher irradiance (Fig. 1d). Event rates rose with both higher $\Delta F/F_0$ and irradiance, resulting in improved signal-to-background ratio (SBR; Fig. 1e, f). Notably, higher irradiance lowered the relative brightness change required to achieve a given SBR, such that higher $\Delta F/F_0$ and irradiance together facilitated higher SBR (Fig. 1g). Collectively, these results suggest that event-based detection can reliably resolve cellular-level dynamics under typical functional imaging conditions (i.e., irradiance = 0.1–1 μW/mm^2, $\Delta F/F_0$ = 10–50%).

Cortical vascular imaging with an event camera

To demonstrate the applicability of event cameras for biological imaging, we first selected a modality that exhibits large brightness fluctuations and rapid dynamics. Cortical vascular imaging satisfies both criteria: the relative fluorescence change ($\Delta F/F_0$) is inherently high due to the weak baseline signal from tissue autofluorescence, and blood flow occurs at millimeter-per-second scales, requiring high temporal resolution to resolve the dynamics accurately. We prepared a mouse cranial window model and intravenously administered FITC-dextran to label blood plasma (Fig. 2a). The anesthetized mouse was secured under a

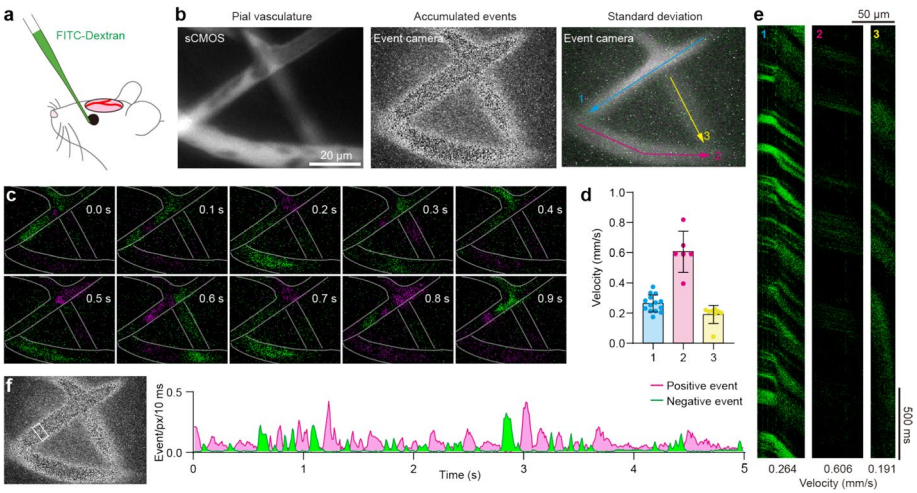

Fig. 2 In vivo cortical vascular imaging using an event camera. **a** Schematic of the mouse preparation. A mouse with a cranial window was anesthetized for cortical imaging. **b** Left, widefield fluorescence image of pial vasculature acquired using an sCMOS camera. Scale bar, 20 μm. Middle, accumulated events from the event camera over time. Right, standard deviation image from naïve accumulation, highlighting three selected regions of interest (ROIs) selected for kymograph-based flow analysis. **c** 100 Hz reconstructed sequential event frames displayed at 0.1s intervals. Positive (green) and negative (magenta) events correspond to RBC-induced brightness fluctuations in narrow vessels. **d** Mean blood flow velocities measured from 1000 Hz reconstructions across the three ROIs. Error bars represent standard deviation over time. **e** Kymographs generated from 1000 Hz reconstructions. Diagonal band slopes correspond to flow velocity. **f** Mean event counts over time from a single vessel ROI (white box in left image). Alternating green and magenta spikes reflect RBC passages through the vessel

custom head-fixation system, and cortical blood flow was imaged through a widefield fluorescence microscope coupled to the event camera.

Narrow cortical vessels were especially well-suited for event-based detection, as trains of red blood cells (RBCs) intermittently displaced the fluorescent plasma, producing strong brightness fluctuations. Event data were initially reconstructed by binning events in 10 ms intervals for visualization, with positive and negative events represented in green and magenta, respectively. Accumulated and standard-deviation images from this reconstruction revealed three vessel branches with clearly resolved blood flow patterns (Fig. 2b). The alternating green and magenta signals at a fixed site correspond to successive RBC passages, consistent with plasma-RBC separation during flow (Fig. 2f).

To achieve higher temporal resolution, we performed reconstruction at 1000 Hz by binning events into 1 ms intervals. Kymographs were generated from selected vessel branches, with slope reflecting flow velocity (Fig. 2d). Flatter slopes correspond to faster RBC movement, while steeper slopes indicate slower flow velocities. For instance, in ROI 1 (cyan, Fig. 2b), slope changes before and after vascular bifurcation indicate localized velocity variation (Fig. 2e). We confirmed that the velocities measured from event-based kymographs were consistent with those obtained from simultaneously recorded sCMOS images in an additional experiment (Fig. S3). These results confirm that event cameras can reliably capture high-speed biological dynamics at frame rates unattainable by sCMOS cameras over the same field of view.

Central principle of implicit neural factorization

To further leverage event cameras for neural activity recording, a robust reconstruction strategy is essential. However, reconstructing calcium imaging from event streams presents a fundamental challenge: the data are sparse and asynchronous, encoding only relative changes in brightness rather than absolute intensities. To overcome this, we developed Implicit Neural Factorization (INF), a reconstruction framework that exploits the intrinsic spatial and temporal structure of calcium signals. Neurons exhibit spatially localized expression of calcium indicators, while neuronal populations show coordinated temporal dynamics [1]. Therefore, events arising from different pixels of the same neuron should be integrated into a unified, continuous-time activity trace —enabling temporal resolution beyond that achievable with fixed time-bin accumulation.

This biological property can be represented through a low-rank factorization [18–20] of calcium imaging data, $L(t) = WH(t)$, with the detailed formulation given by:

$$\begin{bmatrix} l_1(t) \\ l_2(t) \\ l_3(t) \\ l_4(t) \\ \vdots \\ l_s(t) \end{bmatrix} = \begin{bmatrix} w_{11} & w_{12} & \cdots & w_{1k} \\ w_{21} & w_{22} & & w_{2k} \\ w_{31} & w_{32} & \ddots & w_{3k} \\ w_{41} & w_{42} & & w_{4k} \\ \vdots & \vdots & \cdots & \vdots \\ w_{s1} & w_{s2} & & w_{sk} \end{bmatrix} \begin{bmatrix} h_1(t) \\ h_2(t) \\ \vdots \\ h_k(t) \end{bmatrix},$$

where $L(t) \in \mathbb{R}^{s\times 1}$, $W \in \mathbb{R}^{s\times k}$, $H(t) \in \mathbb{R}^{k\times 1}$, and $s \in \mathbb{N}$ and $k \in \mathbb{N}$ denote the number of pixels in the image and the rank of the data, respectively. Here, $l_u(t) \in \mathcal{C}^0\left([t_0, t_f]\right)$ denotes the calcium signal at the u-th pixel in the continuous-time interval $[t_0, t_f]$, $h_v(t) \in \mathcal{C}^0\left([t_0, t_f]\right)$ denotes the temporal signal of the v-th low rank component in the

continuous-time interval $[t_0, t_f]$, and w_{uv} represents the contribution of v-th component to the u-th pixel. To preserve the native temporal precision of event data, temporal components were parameterized as continuous-time functions using implicit neural representation (Fig. 3a) [21, 22]. Each pixel's signal is reconstructed as

$$\widehat{l}_u(t) = \sum_{v=1}^{k} w_{uv} h_{\theta_v}(t),$$

where $h_{\theta_v}(t)$ is a learnable, continuous time function that approximates $h_v(t)$ parameterized by θ, and $\widehat{l}_u(t)$ denotes the predicted signal of the u-th pixel (Fig. 3c).

To design this reconstruction framework, we incorporate the event generation principle: an event occurs when the logarithmic intensity change at a pixel surpasses a fixed threshold, with polarity reflecting signal direction (Fig. 3b) [23]. Based on this, we introduce an Asynchronous Temporal Consistency (ATC) loss [14] that enforces agreement between the temporal intensity changes in the reconstructed signals and the relative increments encoded by the event stream, ensuring physical consistency with the underlying event-generation process. By optimizing this objective under the low-rank formulation, INF learns spatial and temporal components that reconstruct neural activity in continuous-time precision (Fig. 3d; " Methods").

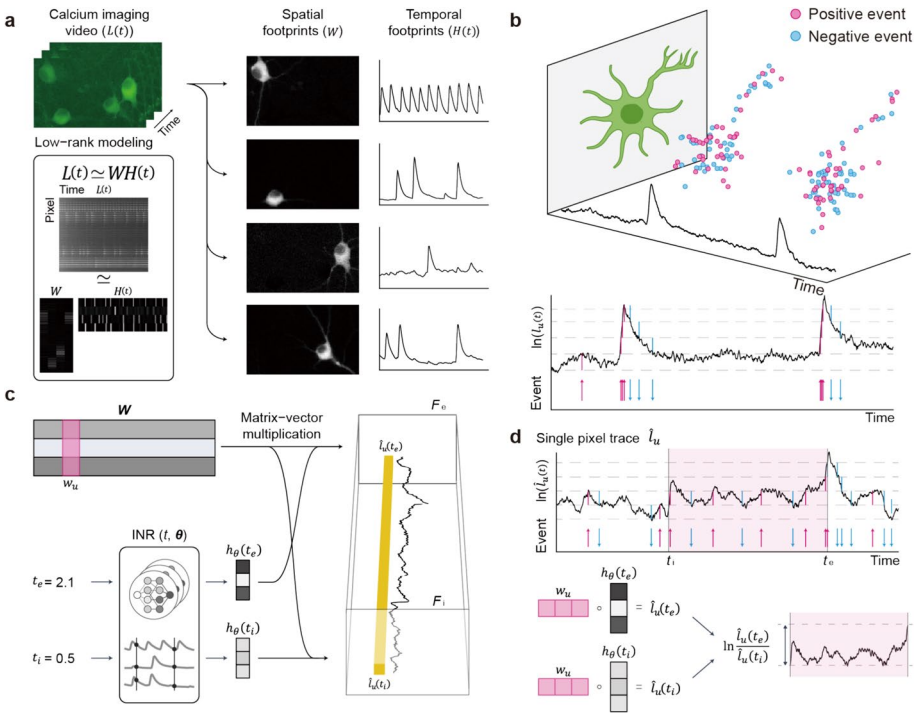

Fig. 3 Reconstruction of event-based calcium imaging via implicit neural factorization (INF). **a** Conceptual overview of INF. Calcium imaging data are factorized into spatial footprints and continuous-time temporal components. **b** Events are generated when the logarithmic change in intensity exceeds a fixed threshold, with polarity indicating the direction of change (pink = positive, cyan = negative). **c** Temporal dynamics are modeled as implicit neural representations and combined with spatial weights to reconstruct continuous calcium signals. **d** A self-supervised loss enforces consistency between predicted temporal intensity changes and accumulated event polarities, ensuring adherence to the physical event-generation process

Reconstruction of calcium signals from in vitro event camera data

To validate the effectiveness of our method in reconstructing calcium signals from experimentally acquired data, we acquired a paired dataset of cultured hippocampal neurons recorded simultaneously with an event camera and an sCMOS camera (Fig. 4a). The data acquired with the sCMOS camera at 10 Hz served as the ground truth. Reconstructions from event data were generated at the same frame rate to allow direct comparison with two representative self-supervised learning-based methods: EvINR [24] and Ev-FlowNet [14]. As shown in Fig. 4b, our approach preserves fine spatial structures that are highly consistent with the sCMOS reference, whereas EvINR and Ev-FlowNet produce noisier reconstructions with a substantial loss of spatial details.

Temporal fidelity was further assessed by extracting ROI traces from the sCMOS recordings and comparing them with reconstructed signals. Our method closely recovers both the amplitude and timing of individual calcium transients, demonstrating strong overlap with the ground-truth traces (Fig. 4c). In contrast, Ev-FlowNet introduces high-frequency noise, while EvINR captures only the coarse trend of the sCMOS signals, with significantly attenuated $\Delta F/F_0$ [1], making individual transients nearly imperceptible.

Quantitative comparisons across three independent recordings are summarized in Fig. 4d. For each dataset, ROI-wise Pearson correlation coefficients (PCCs) were computed between the sCMOS and reconstructed traces. The resulting PCC distributions are displayed as box plots, and statistical significance between methods was assessed using paired t-tests on ROI-level PCC values. Our method consistently outperforms existing approaches, yielding significantly higher correlations ($p < 0.05$) across all datasets.

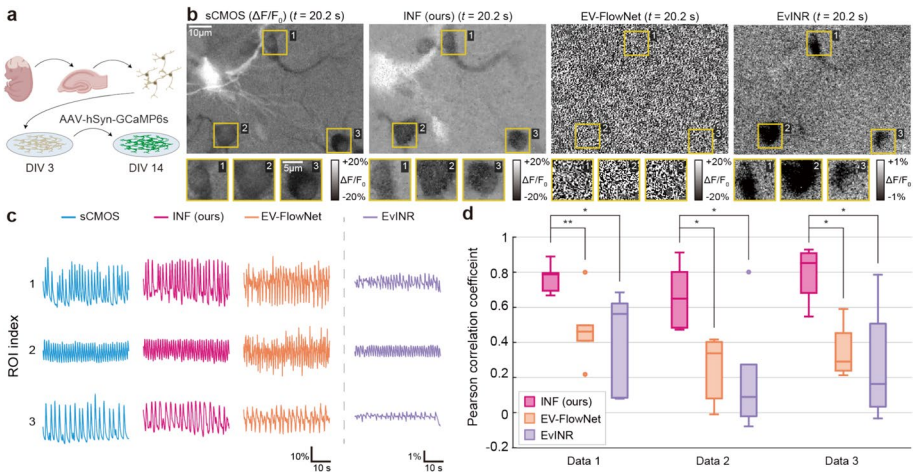

Fig. 4 Comparative evaluation of event-based reconstructions against sCMOS reference. **a** Schematic of the hippocampal neuron culture used for calcium imaging. **b** Example $\Delta F/F_0$ frames reconstructed at 10 Hz; yellow boxes highlight cropped regions shown below at higher magnification. **c** $\Delta F/F_0$ traces from three representative neurons in the sCMOS recording and reconstructions using INF (ours), Ev-FlowNet, and EvINR. INF faithfully captures both the amplitude and timing of individual calcium transients, whereas Ev-FlowNet exhibits noisy fluctuations, and EvINR captures only coarse temporal trends with attenuated amplitudes. **d** Box plots of Pearson correlation coefficients (PCC) between sCMOS recordings and reconstructed traces across all ROIs from three independent datasets. Sample sizes per dataset: $n = 6$, 5 and 4 neurons, respectively. Statistical significance: ns, not significant; * $p < 0.05$; ** $p < 0.01$; *** $p < 0.001$

To further validate the reconstruction framework, we extended the analysis to a larger number of neurons (Fig. 5a). Standard deviation projections from the event-based reconstructions closely matched the sCMOS reference, highlighting overlapping patterns of active neurons (Fig. 5b). Calcium traces extracted from multiple ROIs revealed distinct temporal activity patterns across individual neurons, reflecting heterogeneous activity within the network (Fig. 5c). The reconstructed signals accurately captured both the timing and relative amplitude of these transients compared to the sCMOS recordings, demonstrating that event-based reconstruction can resolve both population-level and subcellular activity in complex, asynchronous networks. These results further confirm the robustness and scalability of our reconstruction framework and its suitability for detailed multi-ROI analysis of calcium dynamics.

Event camera-based imaging of neuronal dynamics in vivo

To further evaluate the applicability of event cameras for imaging calcium dynamics in vivo, we first conducted a feasibility study in brain organoids (Fig. S4). To emulate functional dynamics, we applied synthetic patterned illumination to GFP-expressing neurons in forebrain organoids at a depth of 60 μm from the surface. The illumination pattern was tuned to resemble physiological calcium activity, with fluorescence changes ranging from 20–50% in $\Delta F/F_0$. Individual ROIs were sequentially illuminated at 500 ms intervals and imaged simultaneously with sCMOS and event cameras. Despite signal crosstalk among adjacent ROIs due to tissue scattering, the event camera effectively detected dynamic fluorescence changes, demonstrating its ability to resolve calcium-like activity patterns under scattering environments.

After validating feasibility in organoids, we performed in vivo cortical calcium imaging using event cameras and an upright widefield microscope to assess performance

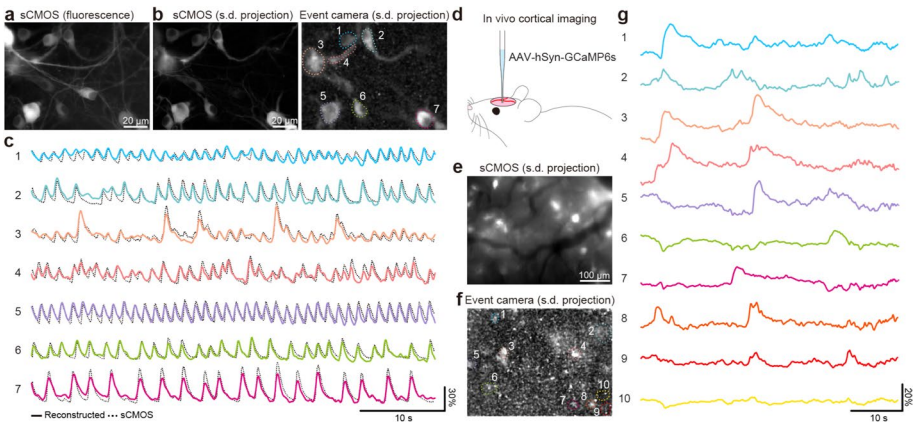

Fig. 5 Event-based imaging and reconstruction of neuronal calcium dynamics. **a** Mean image of the hippocampal neuron culture used for calcium imaging. **b** Standard-deviation projections from the reference sCMOS recording and the event-based $\Delta F/F_0$ reconstructions. A Gaussian blur ($\sigma = 1.5$ pixels) was applied to the event data prior to s.d. computation to suppress sensor-level noise. **c** Calcium traces from selected ROIs in panel **b**. Solid lines represent event-based reconstructions; dotted lines indicate reference sCMOS signals. Both traces were resampled at 10 Hz for comparison. **d** Schematic of the awake mouse model used for in vivo cortical calcium imaging. **e** Standard-deviation projection of the sCMOS signals. **f** Standard-deviation projection from event-based $\Delta F/F_0$ reconstruction, processed identically to **b** (with Gaussian blur applied). **g** $\Delta F/F_0$ traces from selected ROIs shown in panel **f**. Reconstructions were sampled at 10 Hz, and global brightness fluctuations were removed to enhance neuron-specific dynamics

under physiological conditions. A cranial window was prepared in a mouse expressing GCaMP6s in cortical neurons, and imaging was conducted under awake conditions (Fig. 5d). To maximize collection efficiency, sCMOS and event camera recordings were acquired sequentially. Standard-deviation projections from the reconstructed data revealed spatial activity patterns consistent with those captured by the sCMOS camera (Fig. 5e, f). To reduce contamination from global fluorescence fluctuations caused by tissue scattering and deep-layer activity, the global signal component was subtracted from the raw traces, revealing heterogeneous, asynchronous calcium transients across individual neurons (Fig. 5g). Together, these results demonstrate that event cameras faithfully capture in vivo neuronal calcium dynamics with high temporal precision, even under scattering conditions and during awake imaging.

Discussion

With their exceptional temporal resolution, wide dynamic range, and low power consumption and data rates, event cameras represent a promising new modality for biological imaging. Despite these advantages, previous event-based techniques have focused on motion or blinking signals to reconstruct structure or motion. In this study, we successfully visualized vascular dynamics and neuronal calcium activity in both cultured neurons and the cortex of awake mice using event cameras, a significantly more demanding test cases for event cameras with smaller $\Delta F/F_0$ signals and limited irradiance than prior structural or motion-focused applications. The resulting sparse event streams were not readily compatible with conventional quantitative analysis, and existing self-supervised reconstruction methods were insufficient for neuronal functional data, attenuating $\Delta F/F_0$ or introducing strong noise (Fig. 4c, d). To overcome this, we introduced implicit neural factorization (INF), which leverages the spatiotemporal low-rank structure of neural activity to reconstruct $\Delta F/F_0$ traces while preserving sub-millisecond temporal precision. This approach enabled quantitative validation that event cameras can faithfully capture biologically meaningful signals and allowed for direct comparisons with sCMOS recordings.

Several technical refinements could further enhance the performance of event cameras in biological applications. In our setup, the limited illumination area constrained full utilization of the sensor's field of view; intense illumination at the center generated more events than the peripheral regions. This can be addressed by expanding the illumination area or employing a flat-top beam profile to achieve uniform intensity across the field. Furthermore, our widefield configuration shares the intrinsic limitations of single-photon microscopy, including limited depth resolution and background fluorescence. Fortunately, the modular architecture of event cameras enables seamless integration with advanced modalities such as temporal focusing two-photon microscopy [25], spinning disk confocal microscopy, or light-sheet microscopy, which could extend their application to deeper and more specific imaging contexts. This flexibility applies to both imaging modality and hardware selection (Figs. S2 and S3).

The goal of this work was to establish that event-based sensors can be effectively applied to in vivo functional biological imaging, a context in which sCMOS cameras are widely used. In the cortical vessel imaging experiments, we demonstrate a combination of wide field-of-view and 1000 Hz temporal sampling that defines an operational regime

not readily accessible with conventional sCMOS cameras, delineating a complementary capability of event-based sensing beyond standard frame-based acquisition (Fig. 2d, e). Even in regimes where sCMOS systems may approach similar frame rates, event-based sensors provide practical advantages, including compactness and low power consumption, and are beneficial for portable functional imaging platforms.

Therefore, event cameras also hold promise for voltage imaging, where high-speed acquisition is critical. The current limitation arises from the low $\Delta F/F_0$ signals and limited irradiance of existing voltage indicators and genetically encoded voltage indicators (GEVIs), which limit event generation. This limitation could be addressed by developing brighter GEVIs or by incorporating image intensifiers to amplify photon flux without inducing photodamage.

Finally, a notable advantage of event cameras is their ability to detect and correct motion artifacts, owing to their design based on capturing local brightness changes rather than full-frame images. This property, well established in autonomous navigation and robotics, allows for precise motion tracking with high temporal resolution. In biological imaging, this feature can be exploited to detect and mitigate distortions caused by tissue drift, cardiac pulsation, or other physiological movements. Such motion-aware detection enhances signal fidelity and stability during in vivo neural imaging, especially under awake and mobile conditions.

Overall, event cameras represent a compelling platform for high-speed functional imaging in neuroscience. Their combination of asynchronous sensing, continuous-time signal reconstruction via INF, and seamless compatibility with existing optical systems positions them as a versatile tool for capturing rapid biological dynamics**,** particularly those that challenge conventional frame-based imaging.

Conclusion

We established a comprehensive experimental and computational pipeline, encompassing optical characterization, modality validation, and signal reconstruction. Harnessing this framework, we demonstrated that event cameras reliably capture vascular dynamics and neuronal calcium activity in cultured neurons and in the cortex of awake mice. With their high temporal resolution, wide dynamic range, and asynchronous, data-efficient sampling, event cameras offer a powerful and versatile platform for next-generation functional imaging. By enabling real-time, low-latency acquisition of rapid biological signals, they open new avenues for investigating fast neural and vascular dynamics, neuromodulation, and behaviorally relevant activity in vivo.

Methods

Event camera optical setup

The event camera (DVXplorer, iniVation) was mounted on the left port of an inverted epifluorescence microscope equipped with a motorized filter wheel (Eclipse Ti2, Nikon; Fig. 1). An sCMOS camera (Kinetix22, Teledyne Photometrics) was attached to the eyepiece port to enable simultaneous fluorescence imaging. Both cameras and the filter wheel were controlled using NIS-Elements software (Nikon). The light path was adjusted either by an 8:2 beamsplitter (event camera: sCMOS = 8:2) to allow simultaneous acquisition, or by a flip mirror to direct light only to the event camera. Calcium

imaging recordings with sCMOS were acquired at a relatively slow rate (10 Hz) under sufficiently bright illumination, so the sCMOS data were not photon-limited and reliably captured the underlying calcium dynamics despite the 8:2 beam splitter directing less light to the sCMOS camera. For in vivo cortical calcium imaging, the event camera was mounted on the eyepiece port of a custom upright microscope (Cerna, Thorlabs). An sCMOS camera (ORCA-Flash 4, Hamamatsu) was used to define the field of view. In all configurations, a 0.55 × demagnifier (Nikon) was attached to the event camera, increasing its effective field of view by approximately 3.3-fold. The excitation power was set to 0.5–10 $mW{\cdot}mm^{-2}$ for in vitro studies and ~ 30 $mW{\cdot}mm^{-2}$ for in vivo studies. Additional event camera (IMX636, Sony) was used for cross-validation.

Optical characterization

For optical characterization, a single pollen grain was positioned at the center of the field of view. Illumination from a 445-nm LED (Solis-445C, Thorlabs) was modulated at 20 Hz using a LED driver (DC2200, Thorlabs) to generate a triangular waveform. Irradiance was first calibrated by measuring both the direct port output and the sCMOS signal under identical conditions; the sCMOS counts were then used to calculate irradiance during following measurements.

Background events were recorded under stable illumination, and total event counts were measured while varying the illumination amplitude and baseline. Events were collected from a circular ROI corresponding to the size of the pollen grain, and the total number of events was divided by acquisition time to obtain events per millisecond. The corresponding $\Delta F/F_0$ values were calculated from simultaneously acquired sCMOS fluorescence data.

Asynchronous temporal consistency loss

An event is generated at pixel (x, y) when the relative changes in brightness since the previous event reaches a fixed contrast threshold. A positive event occurs when the intensity increases by a factor of $(1 + c)$, and a negative event occurs when it decreases by a factor of $(1 - c)$, where c denotes the linear contrast sensitivity. For two events occurring at the same pixel at time point t_m and t_n $(t_m < t_n)$, the corresponding intensity relationship is expressed as

$$l_u(t_n) = (1 + c)^{\sum p^+}(1 - c)^{\sum p^-} l_u(t_m),$$

where Σp^+ and Σp^- denote the numbers of positive and negative events, respectively. Taking the logarithm yields

$$lnl_u(t_n) - lnl_u(t_m) = \Sigma p^+ ln(1 + c) + \Sigma p^- ln(1 - c).$$

Defining $\theta^+ = ln(1 + c)$ and $\theta^- = ln(1 - c)$, the asynchronous temporal consistency loss [14, 26] is then formulated as

$$\mathcal{L}_{atc} = \Sigma_{u=1}^{s} \Sigma_{n \neq m} \left| (\widehat{lnl}_u(t_n) - \widehat{lnl}_u(t_m)) - (\Sigma p^+ \theta^+ + \Sigma p^- \theta^-) \right|_2^2,$$

which enforces reconstructed signals $\widehat{l}_u(t)$ to remain consistent with the physical event-generation process across all pixels and event pairs.

Regularization and total objective

To promote biologically plausible reconstructions, we impose three regularizations on the spatial component. The sparsity loss $\mathcal{L}_{sp} = |W|_1$ encourages sparsity [27], and the total variation loss $\mathcal{L}_{TV} = |\nabla_x W|_1 + \left|\nabla_y W\right|_1$ promotes spatial smoothness [28]. In addition, a baseline loss L_b is introduced to anchor the reconstruction, which is otherwise ill-posed due to the ambiguity of absolute scale [29].

The total training objective was

$$\mathcal{L}_{total} = \lambda_{atc}\mathcal{L}_{atc} + \lambda_{sp}\mathcal{L}_{sp} + \lambda_{TV}\mathcal{L}_{TV} + \lambda_b L_b,$$

with $\lambda_{atc}, \lambda_{sp}, \lambda_{TV}, \lambda_b$ controlling the respective contributions. To better reflect the structure of calcium imaging data, the spatial component is decomposed as $W = W^s + \mathrm{W^r}$, with regularization applied only to W^s [27]. This design encourages W^s to capture sparse, spatially coherent neuronal footprints, while W^r remains unconstrained to account for background variability.

Pearson correlation coefficient (PCC)

For each ROI r, temporal fidelity is quantified by computing the Pearson correlation coefficient (PCC) between the reconstructed trace and the aligned ground-truth trace. Given reconstructed trace s and ground-truth trace g, the PCC value is defined as

$$\mathrm{PCC} = \frac{\sum_{t=1}^{T}(s-\bar{s})(g-\bar{g})}{T\sigma_s\sigma_g}$$

where $\bar{s}$ and $\bar{g}$ are the mean values of s and g, respectively, and σ_s and σ_g are the standard deviations of s and g.

Preprocessing of sCMOS recordings

To enable direct comparison with event-camera reconstructions, we converted sCMOS videos to the same $\Delta F/F_0$ scale [1]. Prior to $\Delta F/F_0$ computation, we applied a per-pixel linear detrending, consistent with the preprocessing used for the event stream. Specifically, each pixel's fluorescence trace $x_{i,j}(t)$ was modeled with a linear trend and bias, and only the slope was removed, yielding a detrended signal $\widetilde{x}_{i,j}(t)$. The baseline fluorescence F_0 was defined as the temporal mean of this detrended signal, and $\Delta F/F_0$ was computed as $(F\text{-}F_0)/F_0$. Preserving the bias ensured that the denominator remained positive, preventing numerical instabilities when the mean signal approached zero.

Preprocessing of event stream

For each pixel, we constructed an accumulated time series by counting events within successive time bins, followed by linear detrending to remove low-frequency drift arising from sensor offsets and photobleaching (Fig. S5). After detrending, hot pixels [30] that continued to generate excessively frequent events were identified as outliers and excluded by masking samples whose values exceeded a predefined threshold.

Parameterized architecture

The continuous-time signal $L(t)$ is modeled with a low-rank spatiotemporal factorization,

$$L(t) = W^s H^s(t) + W^r H^r(t),$$

where W^s, W^r are nonnegative spatial footprints, and $H^s(t), H^r(t)$ denote temporal dynamics. The temporal components are parameterized using Sinusoidal Representation Networks (SIREN) [21], implemented as two independent models. SIREN is an implicit neural representation model consisting of a multilayer perceptron with sinusoidal activation functions. Spatial footprints were initialized as learnable parameters and constrained to be nonnegative through clamping after each update.

All parameters were optimized using Adam optimizer [31], with learning rates of 1×10^{-5} for temporal and 5×10^{-3} for spatial components. All three datasets in Fig. 4 were trained with the same hyperparameters (rank of $W^s = 40$, rank of $W^r = 10$, $\lambda_{atc} = 15$, $\lambda_{sp} = 0.05$, $\lambda_{tv} = 1 \times 10^{-5}$, and SIREN consisting of three hidden layers of 512 units).

Baseline model configurations

For Ev-FlowNet, we followed the official implementation in events mode. All three datasets in Fig. 3 shared identical hyperparameters: five temporal bins, a learning rate of 0.001, and the Adam optimizer. The only dataset-specific difference was temporal window size, set to 22,000 for Data1, 20,800 for Data2, and 22,300 for Data3.

For EvINR, we used the default configuration provided in the original implementation, except for explicitly setting the event contrast threshold according to the hardware specifications of our event camera. Specifically, the threshold was set to $ln(1.13) \approx 0.122$, corresponding to a 13% relative change in our DVS hardware. A learning rate of 9×10^{-5} was adopted, while the Adam optimizer was retained. All other hyperparameters and training settings remained unchanged.

Primary neuron culture

All animal procedures were approved by the Seoul National University Institutional Animal Care and Use Committee and complied with all relevant ethical regulations for animal research (IACUC #SNU-250515–1, SNU-230703–1–5). Hippocampal primary neuron culture for calcium imaging was conducted following the previously established protocol with modifications [32]. Briefly, hippocampal neurons were dissociated from embryonic day 17–18 (E17–E18) Sprague–Dawley rat pups and plated at a density of 100 cells/mm^2 on 18-mm glass coverslips coated with poly-D-lysine and laminin (Neuvitro, WA). Cells were maintained at 37 °C and 5% CO_2 in NbActiv1 medium (BrainBits) supplemented with 1% penicillin–streptomycin, 1% N-2 supplement. Neurons were sandwich co-cultured with astroglia for developmental support and maintained at 37 °C and 5% CO_2. One-quarter of the culture medium was replaced with fresh medium every 3–4 days. For calcium imaging, neurons were transduced at 4 days in vitro (DIV 4) with AAV-DJ/8-hSyn-GCaMP6s (2.47×10^{13} GC/ml), and imaging was performed 8 days post-infection (DIV 12) at 10 mW·mm^{-2}

using a 25 × silicone-oil immersion objective lens (MRD73250, Nikon; NA = 1.05, working distance = 0.55 mm) during acquisition.

hiPSC culture

The human induced pluripotent stem cell (hiPSC; GM25256, male) was obtained from the National Institute of General Medical Sciences Cell Repository through the Coriell Institute for Medical Research. All hiPSC lines were maintained in 5% CO_2 incubators at 37°C. The hiPSCs were maintained on mitomycin C-treated mouse embryonic fibroblasts (MEFs) and cultured in human hiPSC medium consisting of DMEM/F12 (Gibco) supplemented with 20% KnockOut Serum Replacement (Gibco), 1 × Glutamax (Gibco), 1 × Non-essential amino acids (Gibco), 1% penicillin–streptomycin, 100 μM 2-Mercaptoethanol (Sigma), and 10 ng/mL of human basic FGF (PeproTech). Cells were fed daily and passaged every 5–6 days upon reaching 70% confluency by manual dissection.

Generation of GFP-engineered hiPSC line

The GFP-engineered hiPSC line was genetically engineered using the line GM25256 obtained from Coriell following the previously established protocol with some modifications [33]. In brief, the NEPA electroporator (NEPA21, CUY650P5) was used to perform the electroporation (Poring pulse: voltage 175 V, length 2.5 ms, interval 50 ms, 2 pulses, decay rate 10%, positive polarity; Transfer pulse: voltage 20 V, length 50 ms, interval 50 ms, 5 pulses, decay rate 40%, reverse polarities). 1×10^6 of hiPSCs and 1.8 μg of donor template were mixed with 20 pmol of sgRNA (GGGGCCACUAGGGACAGGAUUGG) and 18 pmol of Cas9 protein (Integrated DNA Technologies (IDT)) and added to NEPA electroporation cuvettes with a 2 mm gap (NEPA). After transfection, 0.5 μg/mL puromycin (Sigma) was added for 10 days, and the medium was changed daily. The gRNA was extracted per colony using DNeasy Blood & Tissue kits (QIAGEN) following clonal expansion, which was then genotyped. The clone used in this study was chosen based on its morphology, homogenous expression of GFP, and the sequence validation of the amplicons.

Generation of forebrain organoids

Forebrain organoids were generated based on previously established protocol with slight modifications [34]. Briefly, colonies were incubated with collagenase IV at 37 °C for 1 h and detached from mitomycin C-treated MEFs. For days 1–6, the embryoid bodies were maintained in DMEM/F12 supplemented with 20% KnockOut Serum Replacement, 1 × Glutamax, 1 × Non-essential amino acids, 1% penicillin–streptomycin, 100 μM 2-Mercaptoethanol, 10 ng/mL of human basic FGF, 2 μM dorsomorphin (Sigma), and 2 μm of A83-01 (Tocris). On day 7, the organoids were embedded in Matrigel (Growth Factor Reduced) with DMEM/F12 supplemented with 1 × Glutamax, 1 × Non-essential amino acids, 1% penicillin–streptomycin, 1 × N-2 supplement (Gibco), and 10 μM SB-431542 (Sigma) for another 7 days. From day 14 onward, forebrain organoids were cultured in a shaking incubator in DMEM/F12 supplemented with 1 × Glutamax, 1 × Non-essential amino acids, 1% penicillin–streptomycin, 100 μM 2-Mercaptoethanol, 1 × N-2 supplement, 1 × B-27 supplement (Gibco), and 2.5 μg/ml Insulin (Sigma). From

day 35, the organoids were further maintained every other day with Matrigel added into the media. Day 50–60 forebrain organoids were imaged for analysis.

Feasibility study in organoids

For the organoid feasibility study, sequential patterned illumination was delivered via a DMD coupled to a blue LED (Solis-445C, Thorlabs; 0.5 $mW{\cdot}mm^{-2}$, 200 ms pulses, 500 ms intervals, sawtooth input). The stimulation sequence and camera triggers were synchronized using a pulse stimulator (Master-9, AMPI). Imaging was performed simultaneously with the sCMOS (10 Hz) and the event camera at ~ 60 μm depth using a 40 × water-immersion objective (N40XLWD-NIR, Nikon; NA = 1.15, working distance = 0.59–0.61 mm). Event camera outputs were naively reconstructed in 100 Hz for analysis.

In vivo imaging

All animal procedures were approved by the Seoul National University Institutional Animal Care and Use Committee (SNU-210607–4–22). Mice were singly housed under a reversed 12:12-h light/dark cycle (22–23 °C, 40–60% humidity) with ad libitum access to food and water. Cranial window surgery was performed as previously described [32]. In brief, wild-type mice were anesthetized with isoflurane (5% induction, 1.5% maintenance), and a 5-mm circular craniotomy was made 2.5 mm caudal and 2.5 mm lateral to bregma. The cortical surface was kept hydrated with saline throughout the procedure.

For calcium imaging, AAV-Syn-GCaMP6s-WPRE (2.47×10^{13} GC/ml) was injected at eight cortical sites (1 mm apart, 50 nl per site, 150 μm depth) at a rate of 50 nl/min. A 5-mm coverslip was sealed over the craniotomy with tissue adhesive, and a steel head bar was fixed using dental cement. Carprofen was administered postoperatively. Imaging was performed in awake mice at ~ 75 μm below the cortical surface using a 10 × objective (MRH00101, Nikon; NA = 0.3, working distance = 16 mm).

For vascular imaging, blood plasma was labeled via intravenous injection of 1% w/v FITC-dextran in PBS (FD2000S, Sigma-Aldrich). Mice were anesthetized with ketamine (100 mg/kg) and dexmedetomidine (1 mg/kg), and anesthesia depth was verified by toe-pinch reflex. Imaging was performed at ~ 75 μm depth using a 40 × water-immersion objective (N40XLWD-NIR, Nikon; NA = 1.15, working distance = 0.59–0.61 mm).

Supplementary Information

The online version contains supplementary material available at https://doi.org/10.1186/s43074-026-00240-8.

Supplementary Material 1: Figure S1. Optical characterization of event camera performance for threshold selection. a, Top, Background event rates measured under stable illumination across different irradiance levels and sensitivity thresholds. Lower thresholds produced more background events. Bottom, Background event rates for all thresholds except the highest. b, Event rates as a function of relative brightness change ($\Delta F/F_0$) and irradiance at different sensitivity thresholds. c, Signal-to-background ratio (SBR) plotted against input $\Delta F/F_0$ and irradiance for each threshold. At the lowest threshold, SBR decreased with increasing irradiance due to excessive background events. Figure S2. Validation of high-speed motion tracking using event-based imaging. a, 5 μm beads were imaged under controlled stage motion using an alternative event-based sensor model (IMX636, Sony) to confirm generalizability and high-speed tracking performance. b, Conventional sCMOS imaging shows motion blur at high speeds. c-d, Event-based imaging reconstructs motion at multiple temporal resolutions (10 ms ≈ 100 Hz; 500 μs ≈ 2 kHz), preserving bead edges and resolving overlapping trajectories. e, Individual bead trajectories were segmented by clustering in events within a 2 ms temporal window. f, Bead velocities were estimated by robust regression of spatiotemporal trajectories. Event-based velocity estimates closely matched the ground-truth stage speed (dashed line; mean: 2.19 ± 0.25 mm/s), confirming accurate, blur-free tracking. Minor inter-bead variations reflect expected differences

in event density during translation. Figure S3. Validation of in vivo capillary blood flow velocity measured with an event-based camera. a, Representative cortical capillaries in the mouse cortex recorded with an sCMOS camera at 100 Hz. The magnified region shows selected line profiles and their corresponding kymographs. b, Simultaneous acquisition from the same field of view using an event-camera recording (IMX636, Sony), reconstructed at 10ms intervals (100 Hz equivalent) to match the sCMOS frame rate. Both imaging modalities exhibit comparable streak patterns in kymographs, representing RBC trajectories. A representative streak at time point t_1 was selected for velocity estimation. c, Event points within a window at t_1 were clustered based on local spatiotemporal velocity, revealing three distinct flow regions corresponding to the annotated line profiles in a and b. d, Velocity measurements for three representative flow paths derived from sCMOS and event-based data show close agreement. e, Correlation between sCMOS- and event-based velocity estimates across 13 streaks from two ROIs confirms robust consistency ($R^2 = 0.86$). Scale bars, 20 μm. Figure S4. Feasibility study for imaging in scattering tissues with brain organoids. a, Generation of the GFP-engineered forebrain organoid for the feasibility study. b, Schematic illustration of the optical configuration. DMDs were used for patterned illumination. c, ROI selection and corresponding patterned illumination representative image acquired with sCMOS. d, Sequential patterned illumination of each ROIs imaged with sCMOS. e, Left, example event acquired with event cameras during sequential patterned illumination. Right, standard deviation image acquired from 100 Hz naïve reconstruction. Gaussian blur of 1 pixel was conducted prior to standard-deviation calculation. f, Sequential patterned illumination of each ROIs imaged with event cameras. Figure S5. Linear detrending for baseline-drift removal in event-derived accumulated signals. a, Accumulated signals (solid) from 18 representative pixels over a 50 s interval with least-squares linear fits (dashed) approximating baseline drift. b, Example detrending results for 4 representative pixels: accumulated signal (blue), fitted linear trend (magenta dashed), and detrended signal (green) obtained by subtracting the fitted trend.

Acknowledgements
This work was supported by the Basic Science Research Program through the National Research Foundation of Korea (NRF), funded by the Ministry of Education, Science, and Technology (RS-2026-25475246, RS-2024-00334680, RS-2024-00436783, RS-2024-00466703, RS-2023-00264409, 2020R1A5A1018081) and a Research Grant from HFSP (RGP003/2024) with the award DOI (https://doi.org/10.52044/HFSP.RGP0032024.pc.gr.194148).

Authors' contributions
E.C., Y-G.Y., and M.C. conceived and initiated this study. K.S., Y-G.Y., and M.C. supervised the research. J.Y. implemented the overall optical system. J.Y. prepared cultured neurons and cranial window models. Soo.H., E.K., I-H.P. and K.S. prepared cortical organoids. J.Y. performed all imaging experiments. S.K., Seu.H., and Y-G.Y. implemented the INF algorithm for reconstruction. M.E. and E-S.C. helped optimize the INF algorithm. F.D.N and E.C. performed and analyzed additional validation and in-vivo imaging. J.Y., S.K., Seu.H., Y-G.Y., and M.C. co-wrote the paper. All authors reviewed and edited the paper.

Data availability
The imaging and experiment data that support the works of this study are available from the corresponding authors on reasonable request.

Declarations

Consent for publication
All authors agreed to publish this paper.

Competing interests
The authors declare no conflicts of interest.

Received: 21 November 2025 Revised: 18 February 2026 Accepted: 13 March 2026
Published online: 25 March 2026

References

1. Grienberger C, Konnerth A. Imaging calcium in neurons. Neuron. 2012;73:862–85.
2. Ahrens MB, Orger MB, Robson DN, Li JM, Keller PJ. Whole-brain functional imaging at cellular resolution using light-sheet microscopy. Nat Methods. 2013;10:413–20.
3. Mandracchia B, Zheng C, Rajendran S, Liu W, Forghani P, Xu C, et al. High-speed optical imaging with sCMOS pixel reassignment. Nat Commun. 2024;15:4598.
4. Hoebe RA, Van Oven CH, Gadella TWJ, Dhonukshe PB, Van Noorden CJF, Manders EMM. Controlled light-exposure microscopy reduces photobleaching and phototoxicity in fluorescence live-cell imaging. Nat Biotechnol. 2007;25:249–53.
5. Kiepas A, Voorand E, Mubaid F, Siegel PM, Brown CM. Optimizing live-cell fluorescence imaging conditions to minimize phototoxicity. J Cell Sci. 2020;133:jcs242834.
6. Hromádka T, DeWeese MR, Zador AM. Sparse representation of sounds in the unanesthetized auditory cortex. PLoS Biol. 2008;6:e16.
7. Rochefort NL, Garaschuk O, Milos R-I, Narushima M, Marandi N, Pichler B, et al. Sparsification of neuronal activity in the visual cortex at eye-opening. Proc Natl Acad Sci. 2009;106:15049–54.

8. Giovannucci A, Friedrich J, Gunn P, Kalfon J, Brown BL, Koay SA, et al. CaImAn an open source tool for scalable calcium imaging data analysis. Elife. 2019;8:e38173.
9. Cabriel C, Monfort T, Specht CG, Izeddin I. Event-based vision sensor for fast and dense single-molecule localization microscopy. Nat Photonics. 2023;17:1105–13.
10. Guo R, Yang Q, Chang AS, Hu G, Greene J, Gabel CV, et al. EventLFM: event camera integrated Fourier light field microscopy for ultrafast 3D imaging. Light Sci Appl. 2024;13:144.
11. He W, Zhu J, Feng Y, Liang F, You K, Chai H, et al. Neuromorphic-enabled video-activated cell sorting. Nat Commun. 2024;15:10792.
12. Wang H, Hadjiivanov A, Blazquez E, Schlepütz CM, Stampanoni M, Lovric G. Event-guided temporally super-resolved synchrotron X-ray imaging. Commun Phys. 2025;8:222.
13. Baird RG, Majumder A, Menon R. Dynamic spectral fluorescence microscopy via event-based & CMOS image-sensor fusion. Opt Express. 2025;33:2169–78.
14. Paredes-Vallés F, Croon GCHE de. Back to event basics: self-supervised learning of image reconstruction for event cameras via photometric constancy. In: 2021 IEEE/CVF Conference on Computer Vision and Pattern Recognition (CVPR). 2021. pp. 3445–54.
15. Scheerlinck C, Rebecq H, Gehrig D, Barnes N, Mahony RE, Scaramuzza D. Fast Image Reconstruction with an Event Camera. In: 2020 IEEE Winter Conference on Applications of Computer Vision (WACV). 2020. pp. 156–63
16. Rebecq H, Ranftl R, Koltun V, Scaramuzza D. High speed and high dynamic range video with an event camera. IEEE Trans Pattern Anal Mach Intell. 2021;43:1964–80.
17. Liu S, Dragotti PL. Enhanced event-based video reconstruction with motion compensation. arXiv preprint arXiv:240311961. 2024.
18. Cho J, Han S, Cho E-S, Shin K, Yoon Y-G. Robust and efficient alignment of calcium imaging data through simultaneous low rank and sparse decomposition. In: 2023 IEEE/CVF Winter Conference on Applications of Computer Vision (WACV). 2023. pp. 1938–47.
19. Pnevmatikakis EA, Gao Y, Soudry D, Pfau D, Lacefield C, Poskanzer K, et al. A structured matrix factorization framework for large scale calcium imaging data analysis. arXiv preprint arXiv:14092903. 2014.
20. Han S, Cho E-S, Park I, Shin K, Yoon Y-G, et al. Efficient Neural Network Approximation of Robust PCA for Automated Analysis of Calcium Imaging Data. In: de Bruijne M, Cattin PC, Cotin S, Padoy N, Speidel S, Zheng Y, et al., editors. Medical Image Computing and Computer Assisted Intervention – MICCAI 2021. Cham: Springer International Publishing; 2021. p. 595–604.
21. Sitzmann V, Martel J, Bergman A, Lindell D, Wetzstein G. Implicit neural representations with periodic activation functions. Adv Neural Inf Process Syst. 2020;33:7462–73.
22. Lindell DB, Van Veen D, Park JJ, Wetzstein G. Bacon: Band-limited coordinate networks for multiscale scene representation. In: Proceedings of the IEEE/CVF conference on computer vision and pattern recognition. 2022. pp. 16252–62.
23. Brandli C, Berner R, Yang M, Liu S-C, Delbruck T. A 240 × 180 130 dB 3 µs latency global shutter spatiotemporal vision sensor. IEEE J Solid-State Circuits. 2014;49:2333–41.
24. Wang Z, Lu Y, Wang L. Revisit event generation model: Self-supervised learning of event-to-video reconstruction with implicit neural representations. In: European Conference on Computer Vision. Cham: Springer; 2024. pp. 321–39.
25. Oron D, Tal E, Silberberg Y. Scanningless depth-resolved microscopy. Opt Express. 2005;13:1468–76.
26. Lichtsteiner P, Posch C, Delbruck T. A 128 × 128 120 dB 15 µs latency asynchronous temporal contrast vision sensor. IEEE J Solid-State Circuits. 2008;43:566–76.
27. Pnevmatikakis EA, Soudry D, Gao Y, Machado TA, Merel J, Pfau D, et al. Simultaneous denoising, deconvolution, and demixing of calcium imaging data. Neuron. 2016;89:285–99.
28. Rudin LI, Osher S, Fatemi E. Nonlinear total variation based noise removal algorithms. Physica D. 1992;60:259–68.
29. Bardow P, Davison AJ, Leutenegger S. Simultaneous optical flow and intensity estimation from an event camera. In: Proceedings of the IEEE conference on computer vision and pattern recognition. 2016. pp. 884–92.
30. Wang Z, Ng Y, van Goor P, Mahony R. Event camera calibration of per-pixel biased contrast threshold. arXiv preprint arXiv:201209378. 2020.
31. Kingma DP, Ba J. Adam: A method for stochastic optimization. In: International Conference on Learning Representations (ICLR). San Diego: ICLR; 2015.
32. Kim S, Yoon J, Ko G, Kang I, Tian H, Fan LZ, et al. Optical segmentation-based compressed readout of neuronal voltage dynamics. Nat Commun. 2025;16:7194.
33. Hong S, Lee J, Kim Y, Kim E, Shin K. AAVS1-targeted, stable expression of ChR2 in human brain organoids for consistent optogenetic control. Bioeng Transl Med. 2024;9:e10690.
34. Kim E, Kim Y, Hong S, Kim I, Lee J, Yoo J-Y, et al. A stepwise, modular design of building uniform brain assembloids representing the dynamic cellular interplay between neurons and glial cells. bioRxiv. 2024:2010.

Publisher's Note